Experimental investigation of vitreous humour motion within a human eye model

Rodolfo Repetto[1], Alessandro Stocchino[2] and Chiara Cafferata[2]

[1] Dipartimento di Ingegneria delle Strutture, delle Acque e del Terreno, University of L'Aquila, Italy
[2] Dipartimento di Ingegneria Ambientale, University of Genova, Italy

E-mail: rodolfo@ing.univaq.it

Abstract

We present an experimental study of the vitreous motion induced by saccadic eye movements. A magnified model of the vitreous chamber has been employed, consisting of a spherical cavity carved in a perspex cylindrical container, which is able to rotate with a prescribed time law. Care has been taken to correctly reproduce real saccadic eye movements. The spherical cavity is filled with glycerol and the flow field is measured on the equatorial plane orthogonal to the axis of rotation, through the PIV technique. Visualizations of the fully three-dimensional flow suggest that it essentially occurs on planes perpendicular to the axis of rotation, the motion orthogonal to such planes being smaller by three to four orders of magnitude. Theoretical results, based on a simplified solution, are in very good agreement with the experimental findings. The maximum value of the shear stress at the wall, which is thought to play a possibly important role in the pathogenesis of retinal detachment, does not significantly depend on the amplitude of saccadic movements. This suggests that relatively small eye rotations, being much more frequent than large movements, are mainly responsible for vitreous stresses on the retina. Results also illustrate the dependence of the maximum shear stress at the wall from the vitreous viscosity.

1. Introduction

The vitreous humour, which is bounded between the lens and the retina, is the substance filling the vitreous chamber of the human eye. Lee *et al* (1992) have studied the rheology of vitreous, showing that, in normal conditions, it behaves as a viscoelastic material. However, typically, with advancing age the vitreous partially or completely loses its elastic properties, as a consequence of a 'liquefaction process'.

Vitreous motion plays an important role in retinal detachment mechanisms. In particular, the so-called rhegmatogenous retinal detachment occurs when a progressive infiltration of liquefied vitreous takes place through a retinal tear, i.e. a break in the retina. This not yet deeply understood mechanism seems to have a purely mechanical nature.

The need for achieving better insight into vitreous motion led Lindner in 1933 to perform hydrodynamic experiments aimed at understanding the structure of the flow field induced by eye rotations within the vitreous chamber. The above experiments were later reconsidered and extended by Rosengren and Östrelin (1976). Both the above authors point out the importance of eye rotations on the vitreous dynamics. However, their works only provide a qualitative picture of the hydrodynamic events within the vitreous chamber because their experimental approach did not permit quantitative measurements of fluid velocity to be performed. Moreover, in order to simplify the experimental conditions, both of the authors modelled the eye as a cylinder while, clearly, a spherical domain better represents the real shape of the vitreous chamber. Finally, in the previous experiments, no attempt was made to take into account the scale effects arising from the magnified size of the eye model.

Greater insight into vitreous motion is provided by the work of David *et al* (1998). The authors studied analytically the motion of a viscoelastic fluid within a periodically rotating sphere, adopting simplifying assumptions on the flow characteristics, whose validity has been tested numerically for the case of a purely viscous Newtonian fluid. Their results clarify most of the features of the flow field, showing, in particular, that the fluid motion in the inner part of the domain is out of phase with respect to the wall motion. Moreover, David *et al* (1998) computed the shear stress at the wall and showed that it increases with the sphere radius. The latter observation was interpreted by the authors as a possible explanation of the more frequent occurrence of retinal detachments in myopic eyes, typically characterized by a larger size.

In the present contribution, we present the results of a series of experiments on vitreous motion. The vitreous chamber has been modelled as a spherical cavity, magnified with respect to the real geometry, carved within a perspex cylinder and able to rotate according to a prescribed time law. The cavity has been filled with glycerol, which is a high viscosity Newtonian fluid; thus, the elastic properties of physiological vitreous are disregarded in this first experimental approach to the problem. However, David *et al* (1998) report that the elastic component plays a fairly minor role on the flow field within the eye globe with respect to the viscous one. Moreover, according to the authors' results, the elastic component of the vitreous behaviour does not influence the maximum shear stress at the wall, which is the most important quantity to be evaluated in order to understand the connection between vitreous motion and retinal detachment. Finally, it is worth noting that after surgery (vitrectomy) the vitreous may be replaced by tamponade fluids, typically silicon oils, which are highly viscous Newtonian fluids. The flow field has been experimentally measured, on the equatorial plane orthogonal to the axis of rotation, through the PIV technique. This has allowed us to obtain the spatial structure of the flow field in such a plane with great detail. Moreover, the time evolution of the flow can also be suitably described.

Two sets of experiments have been carried out. The first one is aimed at verifying the results of David *et al* (1998) for purely viscous fluids; therefore, the eye model is rotated according to a sinusoidal time law. Real saccades have a much more complex time behaviour, though, and can hardly be described in terms of a simple sine function. Therefore, in a second set of experiments, a time law for the container angular velocity has been adopted that correctly reproduces all the features of real large amplitude saccadic movements. Saccades with different amplitudes (from $10°$ to $50°$) have been studied. The second set of experiments provides important insight both into the structure of the flow field occurring within the eye and into the shear stresses exerted by the vitreous on the retina during real saccadic movements.

Flow visualizations have also been carried out, with the purpose of quantifying the magnitude of secondary flows possibly generated by the spherical shape of the domain.

2. Saccadic movements

Eyes are subject to various kinds of movements. In the present paper we are concerned with the so-called *saccadic eye movements* that, due to their characteristics, are by far the most important in inducing vitreous motion within the vitreous chamber.

Metrics of saccadic eye movements are reported in detail in Becker (1989). The author identifies the following basic features of saccadic eye movements: (i) a very high initial angular acceleration (up to $30\,000°$ s^{-2}); (ii) a somewhat less intense deceleration that is nevertheless capable of inducing a very efficient stop of the movement; (iii) a peak angular velocity that rises in proportion to the saccade amplitude up to a saturation value ranging between 400 and $600°$ s^{-1}. Saccade amplitude ranges from $0.05°$ (microsaccades) to 80–$90°$, which is the physical limit for the orbit. Obviously, very large saccades are normally accompanied by head rotations.

A saccade movement is typically described through the following quantities: the saccade amplitude A, the saccade duration D, the peak angular velocity Ω_p and the acceleration time t_p, i.e. the time required to reach the peak velocity starting from rest. Becker (1989) reports that the relationship between saccade duration and saccade amplitude is very well described by the following linear law:

$$D = D_0 + dA, \tag{1}$$

in the range $5° < A < 50°$. In equation (1) D is measured in seconds and A in degrees. According to measurements performed by the author the slope d approximately assumes the value of 0.0025 s deg^{-1} and the intercept D_0 typically ranges between 0.02 and 0.03 s.

The average angular velocity during a saccadic movement is defined as $\overline{\Omega} = A/D$ and measurements suggest that the ratio $\Omega_p/\overline{\Omega}$ between the peak and the mean velocities attains a fairly constant value. Becker (1989) suggests the following estimate:

$$\Omega_p/\overline{\Omega} \sim 1.64. \tag{2}$$

Finally, the experimental data show that small amplitude saccades (smaller than $10°$) follow an almost symmetrical time law, the acceleration time being approximatively equal to $0.45D$. The dimensionless acceleration time t_p/D varies linearly with increasing saccade amplitudes, to the value $t_p/D \sim 0.25$ for saccades of $50°$.

In the present work, in order to reproduce the time law $\theta(t)$, describing the angular displacement of the eye, we employ a fifth degree polynomial function, of the form

$$\theta(t) = c_0 + c_1 t + c_2 t^2 + c_3 t^3 + c_4 t^4 + c_5 t^5. \tag{3}$$

The six coefficients are computed imposing the following constraints: $\theta(0) = 0$, $\theta(D) = A$, $\dot{\theta}(0) = 0$, $\dot{\theta}(D) = 0$, $\dot{\theta}(t_p) = \Omega_p$ and $\ddot{\theta}(t_p) = 0$, where D, Ω_p and t_p are evaluated by the relationships described above and superscript dots denote time derivatives. The resulting functions $\theta(t)$ and $\Omega(t) = d\theta(t)/dt$ are shown in figures 1(a) and (b) and they satisfactorily reproduce the main features of real saccadic movements as reported by Becker (1989) (figure 1, chapter 2, page 14).

3. Experimental set-up and data analysis

The eye globe has been modelled by means of two semi-spherical cavities of 40 mm radius, carved into two halves of a plastic cylinder of external radius equal to 120 mm. The material
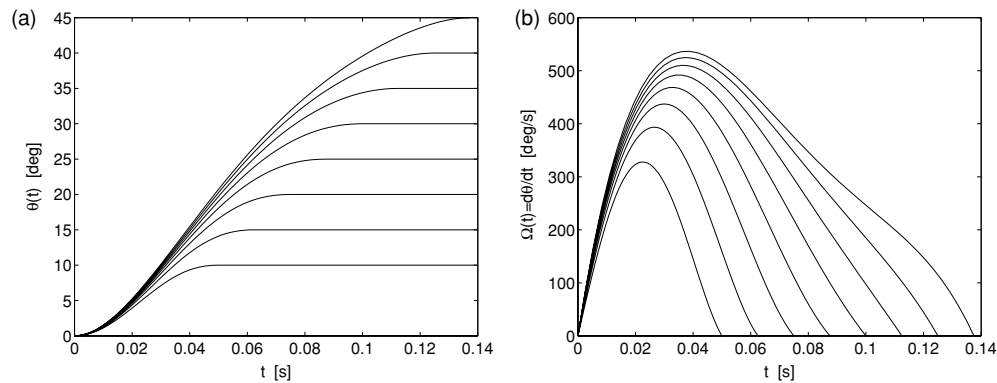
Figure 1. Examples of saccadic eye movements as predicted by equation (3). (a) Angular displacement $\theta(t)$, (b) angular velocity $\Omega(t) = d\theta/dt$ ($D_0 = 0.025$ s, $d = 0.0025$ s/deg).

employed was perspex for the reasons explained below. The spherical cavity was filled with a 98% pure glycerol solution, a highly viscous Newtonian fluid. Due to its strong dependence on the external temperature, the dynamic viscosity of the glycerol solution was periodically measured, using a falling ball viscometer, during each acquisition session in order to continuously monitor its possible variations. Note that the index of refraction of the glycerol matches the index of refraction of the perspex used for the container, thus excluding any deformation in the images due to refraction of light rays when they cross the curved interface between the two materials. The cylinder was mounted on a support directly connected to the shaft of an electrical brushless motor, which allowed the eye model to rotate around its vertical axis, according to an assigned temporal law. In particular, the movement of the eye globe was simulated assigning either a sinusoidal or a polynomial temporal law, see equation (3), the latter representing the human saccadic movements as described in the previous section. The motor was remotely controlled and the actual position was tracked recording the feedback position analog signal. Moreover, the rotation of the shaft was synchronized with a two-dimensional particle image velocimetry (PIV) acquisition system that was employed to measure two-dimensional velocity fields. A cylindrical and a spherical lens converted a laser beam generated by two 30 Hz Nd:Yag lasers into a laser sheet of 0.5 mm thickness and of planar dimensions sufficient to illuminate the area of interest. The laser sheet was aligned with the equatorial plane orthogonal to the axis of rotation using two coated laser mirrors placed on a linear rail. The seeding particles used were hollow glass spheres of mean diameter around 10 μm and a density that matches the density of the working fluid. A sketch of the experimental apparatus is shown in figure 2.

The sampling rate employed in the experimental measurements was set such to obtain 40 vector fields within a period in the case of a sinusoidal movement and 20 flow fields in a single duration of a saccadic movement. Each velocity field ($u(x, y, t), v(x, y, t)$), where $u(x, y, t)$ and $v(x, y, t)$ are the velocity components in the x and y directions respectively, was measured 60 times. An ensemble average ($U(x, y, t), V(x, y, t)$) was then determined and the corresponding root mean square values u_{RMS} and v_{RMS} assumed values of a few per cent of the averaged velocity components U and V. The PIV settings used to analyse the images in terms of cross-correlation yielded to a spatial resolution of about one velocity vector per 1.5 mm^2. Vector fields were transformed into polar coordinates, which is a more natural choice for the geometry of the domain investigated. The velocity components have been interpolated following the method suggested in Agüí and Jeménez (1987) and Stüer and Blaser (2000).
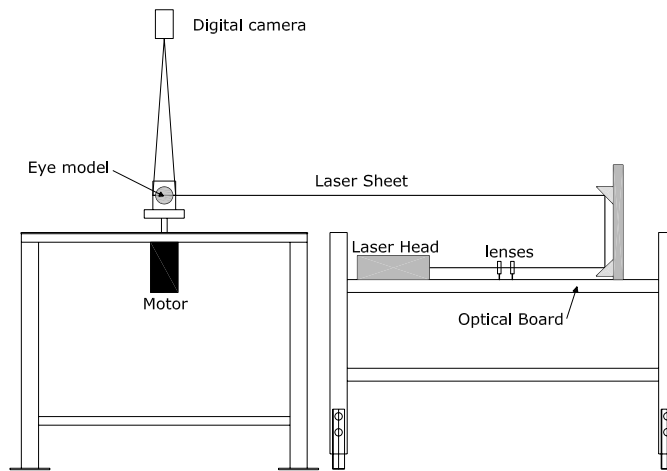
Figure 2. Sketch of the lateral view of the experimental apparatus.
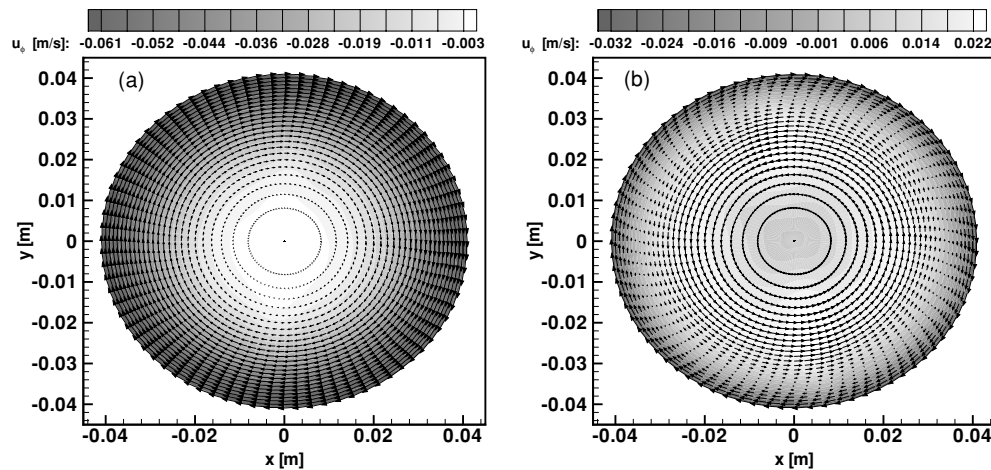

Figure 3. An example of two-dimensional interpolated velocity fields of a periodic experiment ($A = 10°$, $f = 1.75$ Hz) together with contours of the circumferential velocity: (a) velocity field corresponding to the maximum peripheral velocity, (b) velocity field measured immediately after the inversion of the peripheral velocity.

Finally, in view of the axial symmetrical shape of the domain, we have performed an average of the circumferential velocity u_φ along φ. From the measured velocity profiles we have derived tangential stresses, by differentiation of the velocity using a finite least-squares scheme. An example of the two-dimensional interpolated velocity fields is given in figure 3, where two vector fields at different times of a sinusoidal experiment are shown together with contours of the circumferential velocity u_φ.

4. Flow visualization

As described in the previous section, we have performed two-dimensional measurements of the velocity field on the equatorial plane orthogonal to the axis of rotation. Such a plane is a
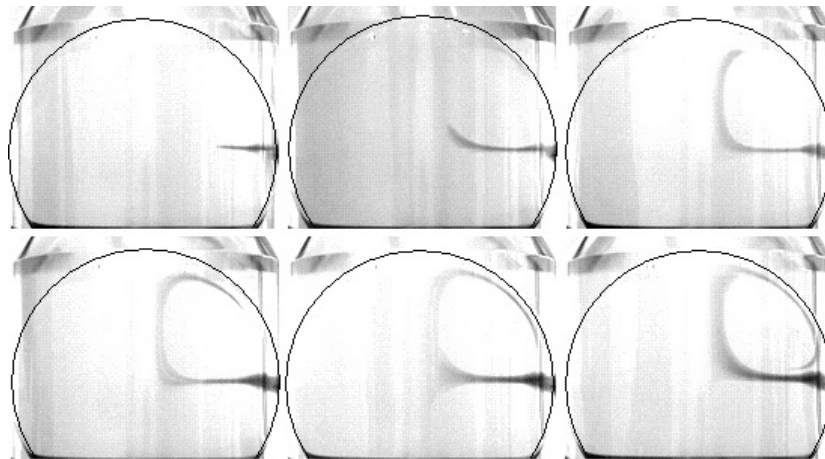
Figure 4. Snapshots of vertical planes, in false colours, at different times of the visualization in a periodic experiment. Time grows from top left to bottom right, the time interval between two successive frames is 8 s, which corresponds to 20 periods of the sinusoidal rotation ($A = 20°$, $f = 2.5$ Hz).

plane of symmetry of the motion; therefore, one expects the velocity vectors to lie on it. In order to gather information on the three-dimensional structure of the flow field, we have also performed a series of flow visualizations, both rotating the eye model with a periodic time law and with a series of saccadic movements. Flow was visualized by injecting a coloured dye close to the wall, just above the equatorial plane. The evolution of the dye streak inside the domain was recorded by means of a digital camera. In figure 4 frames of vertical planes at different times are shown for a periodic experiment. It appears that, in addition to the motion on horizontal planes, which is forced by the boundary condition at the wall, a 'secondary flow' takes place, consisting of two toroidal vortices, located in the northern and southern hemispheres, respectively. The sense of rotation of such vortices is such that, in the upper hemisphere, particles close to the equatorial plane move towards the globe centre, then proceed upwards to descend back close to the curved wall. Such a secondary flow, which had been found numerically by David *et al* (1998), has been invariably observed, both for periodic and saccadic movements. Its intensity, however, is at least three to four orders of magnitude smaller than that of the circumferential flow in the case of periodic rotations and even smaller for saccadic movements.

5. Theoretical background

David *et al* (1998) have proposed a simplified analytical model for the motion of a visco-elastic fluid within a periodically rotating sphere, which will shortly be described in the following for the case of a purely viscous fluid. The authors assume that the flow field is axis-symmetrical, as a consequence of the symmetry of the domain, and that the velocity vectors lay anywhere on planes perpendicular to the axis of rotation. Let us consider a system of spherical coordinates (r, ϑ, φ), with ϑ and φ the elevation angular coordinate and the azimuthal coordinate, respectively. Let us also assume that the sphere rotates about the vertical axis $\vartheta = 0, \pi$. If the flow field is described in terms of the corresponding velocity components $(u_r, u_\vartheta, u_\varphi)$ the simplifying assumptions adopted by David *et al* (1998) imply

that $u_r = u_\vartheta = 0$ and that u_φ does not depend on φ. Note that the above assumptions can be formally justified on a mathematical ground only in the case of small values of the Reynolds number, i.e. when the nonlinear terms in the Navier Stokes equations can be neglected. In the experiments performed in the present work the Reynolds number (computed adopting the maximum wall velocity and the sphere radius) ranges between 1 and 10. This implies that the above assumptions are not strictly mathematically justified. However, as described in the previous section, visualizations of the flow field have shown that the vertical component of the velocity (i.e. the out-of-plane component) is three to four orders of magnitude smaller than the primary flow taking place on horizontal planes, both in the case of periodic rotations and in the case of saccadic movements. This provides a justification for the assumptions adopted in the theoretical model. Using the above scheme the φ component of the momentum equation may be written as:

$$\frac{\partial u_\varphi}{\partial t} = \nu \left[\frac{1}{r^2} \frac{\partial}{\partial r} \left(r^2 \frac{\partial u_\varphi}{\partial r} \right) + \frac{1}{r^2 \sin \vartheta} \frac{\partial}{\partial \vartheta} \left(\sin \vartheta \frac{\partial u_\varphi}{\partial \vartheta} \right) - \frac{u_\varphi}{r^2 \sin^2 \vartheta} \right], \qquad (4)$$

with the boundary conditions

$$u_\varphi = F(t) \sin \vartheta \qquad (r = R), \qquad (5)$$

$$u_\varphi = 0 \qquad (r = 0), \qquad (6)$$

where ν denotes the kinematic viscosity and R is the sphere radius.

David *et al* (1998) considered the case of periodic rotations of the sphere with frequency ω, seeking a separable solution of the form:

$$u_\varphi = e^{i\omega t} g(r) \sin \vartheta + \text{c.c.}, \qquad (7)$$

where c.c. denotes the complex conjugate and the dependence of the solution from $\sin \vartheta$ arises from the boundary condition at the wall (5). The solution for the function g is found in the following form:

$$g(r) = c j_1(kr), \qquad (8)$$

where j_1 is the spherical Bessel function of the first kind and of order 1. The coefficient k in equation (8) is defined as

$$k = \frac{\sqrt{2}}{2} (1 - i) \sqrt{\frac{\omega}{\nu}}. \qquad (9)$$

The constant c can be determined imposing the boundary condition at the side wall and takes the following values:

$$c = \frac{1}{2 j_1(kR)}, \qquad (10a)$$

$$c = -\frac{i}{2 j_1(kR)}, \qquad (10b)$$

depending on whether $F(t)$ is equal to $\cos(\omega t)$ or $\sin(\omega t)$.

Obviously, as pointed out by David *et al* (1998), the above basic solution can be used to build up more complicated ones induced by sphere rotations which are not sinusoidal in time. Indeed, periodic functions $F(t)$, with period T, can be Fourier decomposed in the form

$$F(t) = c_0 + \sum_{n=1}^{\infty} c_n \cos \left(\frac{2\pi n}{T} t \right) + s_n \sin \left(\frac{2\pi n}{T} t \right). \qquad (11)$$

In the present case, in order to reproduce saccadic eye movements, we have employed a time law consisting of a sequence of rotations described by the fifth-order polynomial function (3) followed by a period of no motion long enough to allow for a complete stop of the fluid motion. In this case, the coefficients c_0, c_n and s_n can be readily determined analytically (though we do not report them here for the sake of brevity) and the solution for the φ component of the velocity can be written in the form:

$$u_\varphi = \sin\vartheta \left\{ c_0 r/R + \sum_{n=1}^{\infty} c_n \left[e^{2\pi i n t/T} \frac{1}{2 j_1(k_n R)} j_1(k_n r) + \text{c.c.} \right] \right.$$
$$\left. + s_n \left[-e^{2\pi i n t/T} \frac{i}{2 j_1(k_n R)} j_1(k_n r) + \text{c.c.} \right] \right\}. \tag{12}$$

6. Experimental results and discussion

In the experiments a magnified model of the vitreous chamber has been employed; therefore, scale effects need to be properly accounted for. If we make equation (4) dimensionless, scaling u_φ by $\Omega_p R$ (with Ω_p being the peak angular velocity), t by T (with T a characteristic time scale of globe rotation) and r by R, it is readily found that the only dimensionless parameter relevant for the problem reads:

$$W = \sqrt{\frac{R^2}{\nu T}}. \tag{13}$$

Physically, the above dimensionless number represents the ratio between a characteristic length scale of the domain (R) and the thickness of the boundary layer at the wall, which is of order $\sqrt{\nu T}$. In the case of periodic rotations it is a natural choice to assume $1/\omega$ as the characteristic time scale and W reduces to the usual Womersley number, as appears in David *et al* (1998) for the purely viscous flow.

We have therefore chosen to preserve the same value of W in the prototype, denoted by the subscript P, and the model. Thus we impose

$$\frac{R^2}{\nu T} = \frac{R_P^2}{\nu_P T_P}. \tag{14}$$

In our case $R = 40.8$ mm. The glycerol viscosity has been measured in each experiment. Moreover, we have assumed $R_P = 12$ mm and $\nu_P = 1.4 \times 10^{-4}$ m^2 s^{-1}, as suggested by Lee *et al* (1992). Once a particular eye movement has been selected equation (14) allows us to determine a relationship between T and T_p, i.e. the scaling of time.

6.1. Periodic movements

In the first set of experiments the eye model was rotated according to a sinusoidal law. The main goal of this series of experiments was to validate the experimental apparatus under relatively simple conditions and verify the feasibility of theoretical results obtained through the approach proposed by David *et al* (1998) and described in the previous section. Note, moreover, that a sinusoidal rotation may be thought of, in a highly simplified way, as a sequence of saccadic movements with alternate directions and with a duration of half the period of rotations (see figure 1(a)). In table 1, the relevant parameters of the whole set of the periodic experiments performed are reported.

In figures 5(a) and (b) the experimental profiles of the averaged circumferential velocity along the radial direction are plotted at different times for experiments sin-10 and sin-16.
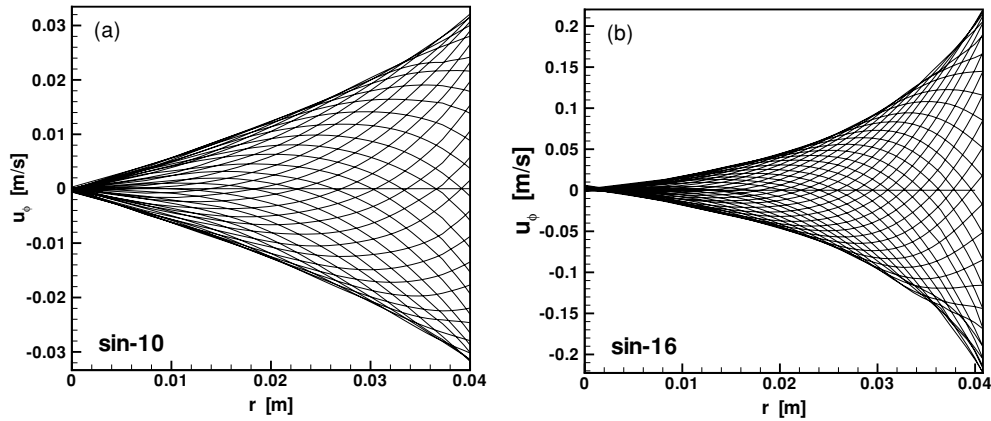
Figure 5. Experimental profiles of the averaged circumferential velocity u_φ along the radius at different times, with interval equal to 1/40 of the period. (a) Experiment sin-10 ($W = 3.75$, $T = 1.33$ s); (b) experiment sin-16 ($W = 5.80$, $T = 0.4$ s).

Table 1. Main parameters of the periodic experiments.

Exp. no.	A (°)	f (Hz)	ν (10^{-4} m^2 s^{-1})	W
sin-1	10	1.0	3.79	5.25
sin-2	20	1.0	6.58	3.99
sin-3	5	1.0	6.25	4.10
sin-4	10	0.5	6.79	2.77
sin-5	10	1.25	7.16	4.27
sin-6	30	1.0	6.73	3.94
sin-7	40	1.0	6.50	4.01
sin-8	10	1.5	6.11	5.07
sin-9	10	1.75	6.26	5.41
sin-10	10	0.75	5.58	3.75
sin-11	20	1.5	6.29	5.0
sin-12	10	2.0	6.87	5.52
sin-13	10	2.5	6.94	6.14
sin-14	5	1.0	7.33	3.79
sin-15	10	1.25	7.37	4.21
sin-16	20	2.5	7.76	5.80
sin-17	10	2.0	6.64	5.61
sin-18	10	1.5	7.22	4.66
sin-19	10	1.75	7.13	5.01
sin-20	20	1.5	7.08	4.71
sin-21	10	2.5	6.98	6.12

In agreement with results shown by David *et al* (1998) it appears that a significant phase lag characterizes the motion of fluid in the most internal regions relative to the motion at the wall. It also appears that, for larger values of the Womersley number (experiment sin-16), the oscillating boundary layer at the wall is narrower and the fluid particles in the most inner region are subject to small amplitude oscillations. As far as the Womersley number decreases (experiment sin-10) the envelope of the velocity profiles progressively tends to a linear shape.

In figure 6 the amplitude of speed oscillations, scaled by its maximum value, is reported as a function of the dimensionless radial coordinate r/R for some experiments. Referring to the notation employed in section 5 the curves in figure 6 represent the modulus of the
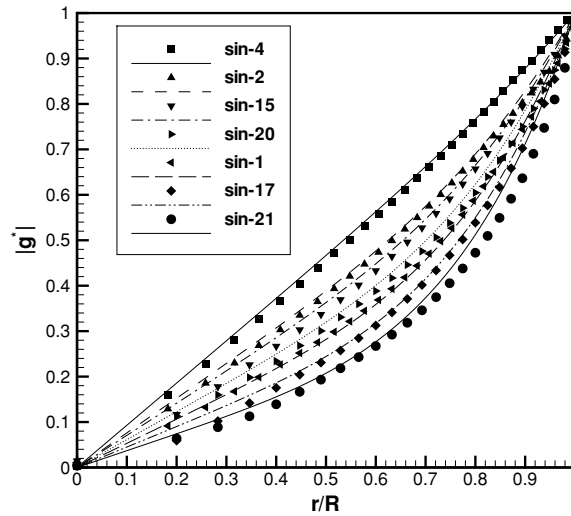
Figure 6. Radial profiles of the dimensionless function $|g^*| = |g|/|g(R)|$, with g defined in equation (8), for different runs. Symbols represent experimental measurements and continuous lines the corresponding theoretical distributions.
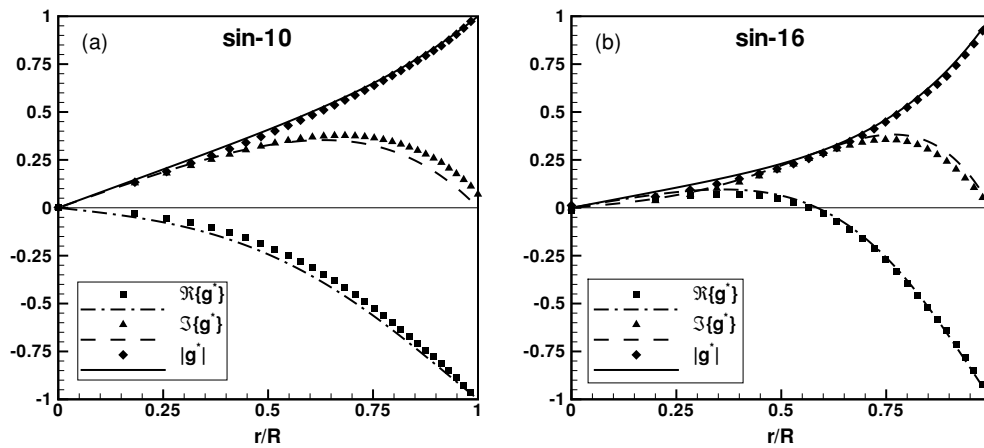

Figure 7. Comparison between the experimental and theoretical distributions of the functions $|g^*| = |g|/|g(R)|$, its real part $\text{Re}\{g^*\}$ and its imaginary part $\text{Im}\{g^*\}$. Symbols denote experimental data, continuous lines theoretical predictions.

dimensionless function $g^* = g(r)/|g(R)|$. Each profile is associated with a different value of W, varying from 2.77 (experiment sin-4) to 6.12 (experiment sin-21). The agreement between measurements and theoretical predictions is good for all values of W. Weak discrepancies may be partly due to the simplified assumptions adopted in the theoretical model and partly to measurement errors, which are estimated to be of 3–4%. Comparison is satisfactory for each experiment though we do not report all data in the figure for the sake of clarity.

A more detailed comparison is shown in figures 7(a) and (b) for experiments sin-10 and sin-16. In this case both the real Re and imaginary Im parts of the dimensionless function g^* are plotted. Note that the ratio $\text{Im}\{g^*\}/\text{Re}\{g^*\}$ is equal to $\tan\phi$, where ϕ denotes the phase lag

Table 2. Main parameters of the experiments on saccadic movements.

Exp. no.	A (deg)	Model			Prototype	
		D (s)	Ω_p (deg s^{-1})	ν (10^{-4} m^2 s^{-1})	D (s)	Ω_p (deg s^{-1})
sac-1	10	0.1024	160.11	7.9	0.050	328.0
sac-2	15	0.1297	189.70	7.8	0.0625	393.6
sac-3	20	0.1536	213.48	7.9	0.075	437.33
sac-4	25	0.1793	228.73	7.9	0.0875	468.57
sac-5	30	0.2023	243.20	8.0	0.10	492.0
sac-6	35	0.2334	245.91	7.8	0.1125	510.22
sac-7	40	0.2529	259.42	8.0	0.1250	524.80
sac-8	45	0.3007	245.41	7.4	0.1375	536.73
sac-9	50	0.3468	236.45	7.0	0.1375	546.67
sac-10	30	0.2043	240.77	7.92	0.10	492.0
sac-11	40	0.2470	265.58	8.19	0.1250	524.80
sac-12	20	0.1428	229.69	8.5	0.0750	437.33
sac-13	10	0.1018	161.12	7.95	0.050	328.0
sac-14	15	0.1386	177.54	7.3	0.0625	393.60

with respect to the wall motion at each point in the radial direction. The agreement between measurements and theoretical predictions appears quite satisfactory.

6.2. Saccadic movements

Let us now consider the experiments performed employing the time law (3). The duration of a saccadic movement is computed adopting equation (1) and the corresponding duration of the motion in the experiment is obtained multiplying D by the factor $(R/R_P)^2 \nu_p/\nu$. Each saccadic movement is followed by a time of rest with a duration of five times the saccade duration, thus allowing a complete stop of the fluid motion. The whole set of experiments performed is reported in table 2; each experiment corresponds to a rotation with a different amplitude.

In figures 8(a) and (b) the experimental velocity profiles along the radial direction are reported at different times for experiments sac-12 and sac-11 which reproduce a small amplitude (10°) and a large amplitude (40°) saccade. It appears that, starting from rest, fluid motion is initially confined within a narrow region close to the wall and the thickness of such a region increases with time. During the acceleration phase of duration t_p, velocity profiles have the same concavity and the velocity attains its maximum at the wall (solid lines). During the phase of deceleration of the wall, the maximum of the velocity detaches from the boundary and progressively moves towards the centre (dashed lines). At the time $t = D$ the wall stops and dissipations smooth down the velocity profile until the fluid is at rest again (the last profile shown in figure 8 refers to a time lower than $2D$ and a complete stop of the motion has not occurred yet). During the decay phase velocity profiles become more symmetrical because the maximum velocity moves towards the point $r = R/2$.

In figures 8(c) and (d) the shear stress $\tau_{r\varphi}$, corresponding to velocity distributions shown in figures 8(a) and (b), is reported. The shear stress is computed according to the relationship

$$\tau_{r\varphi} = \mu \left(\frac{\partial u_\varphi}{\partial r} - \frac{u_\varphi}{r} \right), \tag{15}$$

directly from the experimental data. In the above relationship μ represents the dynamic viscosity of the fluid. It appears that, during a saccadic movement, the wall is subject both to
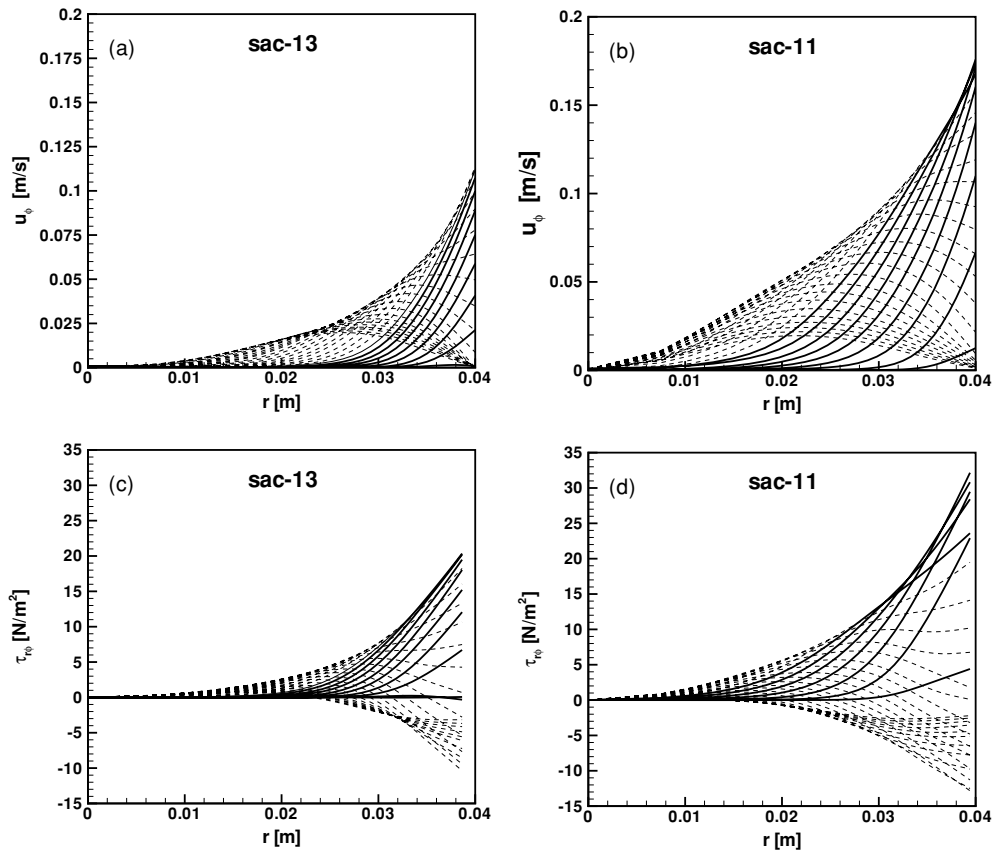
Figure 8. Experimental profiles of the averaged circumferential velocity ((a) and (b)) along the radius at different times with interval equal to $1/20$ of the saccade duration D. Corresponding profiles of the shear stress $\tau_{r\varphi}$ along the radius at different times ((c) and (d)). (a) and (c): Run sac-13 ($D = 0.1018$ s); (b) and (d): run sac-11 ($D = 0.2470$ s). Solid lines correspond to profiles measured during the acceleration phase of the saccade ($t \leqslant t_p$), while dashed lines to profiles measured during the deceleration phase.

positive and negative shear stresses, though the maximum shear stress at the wall is invariably positive. In other words, quite intuitively, the fluid acts at the boundary with stresses mainly in the opposite direction with respect to the wall motion.

In figure 9(a) the maximum velocity scaled by the corresponding maximum velocity at the wall $\Omega_p R$ is plotted versus the dimensionless radial coordinate r/R. Each curve corresponds to a saccade with a different amplitude. Continuous lines represent results obtained through the theoretical solution (12). As for the case of sinusoidal motion the agreement is good for all experiments, though the theory slightly overestimates the maximum velocities. In figure 9(a) only a few experiments have been reported for the sake of clarity, the agreement with the observations being good for the whole set. This figure suggests that the envelope of the velocity profiles is thicker for larger saccades: small saccades induce in the interior part of the domain a motion weaker than the motion driven by larger saccades. This is mainly due to the fact that larger saccades are longer and the boundary layer starting at the wall has more time to grow.
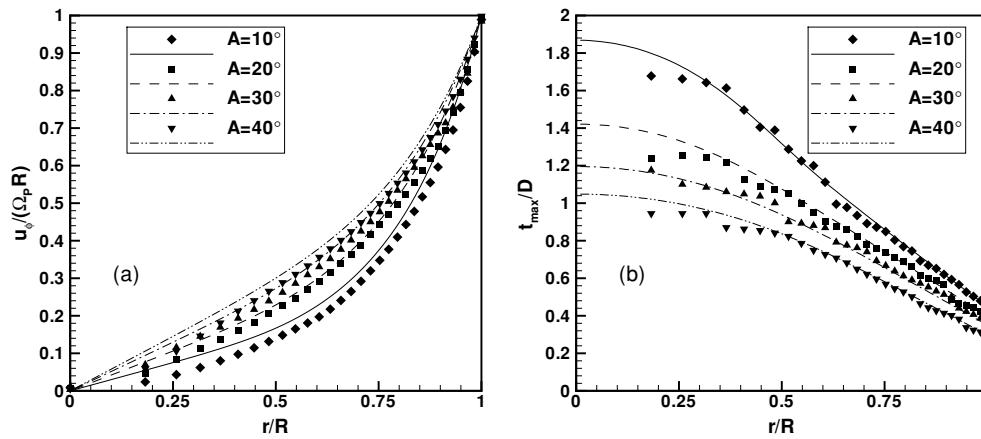
Figure 9. (a) Dimensionless maximum value reached in time by the circumferential velocity u_φ at each point in the radial direction for different experiments. (b) Dimensionless time t_{max}/D at which the maximum tangential velocity is reached at each point in the radial direction for different experiments. Symbols denote experimental data, lines theoretical predictions.

In figure 9(b) we report the dimensionless time t_{max}/D at which the maximum value of velocity is attained, for each value of r/R. The agreement appears fairly good; the weak irregularity of experimental data is due to the relatively coarse temporal discretization of the saccadic movement (20 flow fields have been measured during a saccade duration). Note that the agreement is less satisfactory in the inner part of the domain; this is due to the fact that in such a region the velocity is very small and affected by a greater relative experimental error. Obviously, at the wall ($r/R = 1$) the maximum velocity is attained at the acceleration time, so that $t_{max} = t_p$. It appears that the more one moves towards the centre of the sphere the larger is the time when the maximum velocity occurs.

As the agreement between theoretical predictions and experimental results has proved to be satisfactory for all the experiments we now proceed to employ the theoretical model to obtain some information on problems which are of potential clinical relevance. Let us first consider the dependence of the maximum shear stress at the wall τ_{max} from the saccade amplitude. In figure 10(a) the dimensional value of τ_{max} is plotted versus the saccade amplitude A. All quantities refer to the prototype, i.e. to the real scale eye. The three curves are relative to different values of the kinematic viscosity of the fluid. In all cases it appears that the maximum shear stress at the wall does not strongly depend on the amplitude of eye rotations. This result, which is not obvious, bears some practical importance. Indeed, small amplitude saccadic movements are, by far, more frequent than large ones. Therefore, according to the present results, small amplitude eye rotations stress the retina more than large movements and should be regarded as the most potentially dangerous.

Finally, in figure 10(b) the dependence of the maximum shear stress at the wall τ_{max} is plotted versus the viscosity of the fluid for different saccade amplitudes. Kinematic viscosity ν ranges between 10^{-6} (approximatively the viscosity of the completely liquefied vitreous) and 5×10^{-3} (relative to the most viscous silicon oil employed during vitrectomy). The figure shows that τ_{max} significantly increases with the fluid viscosity up to a value, for the most viscous case, which is more than twice than that reached in the physiological case ($\nu \sim 10^{-4}$). Thus, from a purely mechanical point of view, in order to minimize the stresses on the retina it would be preferable to employ low viscosity tamponade fluids.
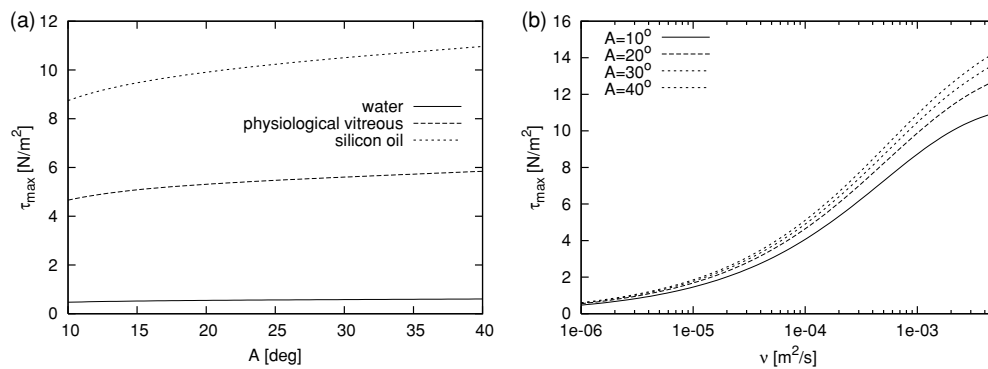
Figure 10. (a) Dependence of the maximum shear stress at the wall τ_{max} from saccade amplitude A for different fluid viscosities (water $\nu = 10^{-6}$ m^2/2, vitreous $\nu = 1.4 \times 10^{-4}$ m^2/2, silicon oil $\nu = 10^{-3}$ m^2/2). (b) Maximum shear stress at the wall τ_{max} as a function of the kinematic viscosity of the fluid ν for different saccade amplitudes.

7. Conclusions

The present work represents the first attempt to measure the flow field induced by saccadic eye movements on a model of the vitreous chamber. Mechanical problems related to vitreous dynamics are extremely complicated, but certainly worth being studied, especially in connection with the occurrence of retinal detachment. As it often happens in attempting to model biological systems it is necessary to resort to fairly idealized approaches and then eventually proceed to progressively complicate the scenario. This was the aim of the present work which is based on the following main simplifying assumptions: the vitreous chamber has been considered a rigid spherical cavity and the vitreous body has been modelled as a purely viscous homogeneous fluid. Even in the quite simple conditions considered here, information which are potentially relevant from the clinical point of view have been obtained.

The second set of experiments, in which real saccadic movements were reproduced, provides a useful insight into the flow field within the vitreous chamber. In particular, it has been shown how fluid motion is generated at the wall, how it spreads towards the centre of the domain and, finally, how it is dissipated. Shear stresses have also been evaluated from the experimental data. It has also been shown that the maximum shear stress at the wall is not strongly dependent on the saccade amplitude. This implies that small amplitude eye rotations, being by far more frequent than large ones, are mainly responsible for the generation of stresses on the retina. Moreover, it has been found that the maximum shear stress at the wall significantly increases with the fluid viscosity; thus, from a purely mechanical point of view, low viscosity tamponade fluids should be adopted after vitrectomy, in order to minimize the stresses on the retina.

Future research should, in our opinion, account for the further complicating effects listed below.

(i) The real shape of the vitreous chamber is not perfectly spherical because, typically, the antero-posterior axis is shorter than the others and particularly due to the presence of the lens in the anterior part. From the fluid dynamical point of view the non-sphericity of the domain may significantly modify the flow field characteristics. This topic has been recently addressed theoretically by Repetto (2005) in the limit of low viscosity fluid but the problem remains open.

(ii) The vitreous in physiological conditions is a visco-elastic fluid. Even if indications exist that the elastic component plays a fairly minor role with respect to the viscous one it would be worthwhile performing experiments employing visco-elastic fluids.

(iii) Strongly myopic eyes, which are most frequently subject to retinal detachment, are elongated in the antero-posterior direction. From the analysis of some echographies of human myopic eyes, we have observed that the antero-posterior axis can be larger than the other axes by 30–40%. The intensities of the tangential stress along the boundary, i.e. the retina, may be significantly affected by the ellipsoidal shape of the eye. Investigation of the flow field within a domain so deformed may provide a sound interpretation of the most frequent occurrence of retinal detachments in myopic eyes.

Acknowledgments

References

Agüí J C and Jiménez J 1987 On the performance of particle tracking *J. Fluid Mech.* **185** 447–68

Becker W 1989 *The Neurobiology of Saccadic Eye Movements* ed R H Wurtz and M E Goldberg (Amsterdam: Elsevier Publisher BV—Biomedical Division)

David T, Smye S, Dabbs T and James T 1998 A model for the fluid motion of vitreous humour of the human eye during saccadic movement *Phys. Med. Biol.* **43** 1385–99

Lee B, Litt M and Buchsbaum G 1992 Rheology of the vitreous body. Part I: viscoelasticity of human vitreous *Biorheology* **29** 521–33

Lindner K 1933 Über die Herstellung von Modellen zu Modellversuchen der Netzhautabhebung *Klin. Mbl. Augenheilk* **90** 289–00

Repetto R 2005 An analytical model of the dynamics of the liquefied vitreous induced by saccadic eye movements *Meccanica* at press

Rosengren B and Östrelin S 1976 Hydrodynamic events in vitreous space accompanying eye movements *Ophtalmologica* **73** 513–24

Stüer H and Blaser S 2000 Interpolation of scattered 3D PTV data to a regular grid *Flow Turbulence Combust.* **64** 215–32